BIOCHEMISTRY
including biophysical chemistry & molecular biology

Article

pubs.acs.org/biochemistry

Inhibition of the *dapE*-Encoded *N*-Succinyl-L,L-diaminopimelic Acid Desuccinylase from *Neisseria meningitidis* by L-Captopril

Anna Starus,[†] Boguslaw Nocek,[‡] Brian Bennett,[§] James A. Larrabee,[∥] Daniel L. Shaw,[∥] Wisath Sae-Lee,[∥] Marie T. Russo,[∥] Danuta M. Gillner,[⊥] Magdalena Makowska-Grzyska,[‡] Andrzej Joachimiak,[*,‡] and Richard C. Holz[*,#]

[†]Department of Chemistry and Biochemistry, Loyola University-Chicago, 1068 West Sheridan Road, Chicago, Illinois 60626, United States

[‡]Center for Structural Genomics of Infectious Diseases, Computation Institute, University of Chicago, 5735 South Ellis Avenue, Chicago, Illinois 60637, United States

[§]Department of Physics, Marquette University, Milwaukee, Wisconsin 53201, United States

[∥]Department of Chemistry and Biochemistry, Middlebury College, Middlebury, Vermont 05753, United States

[⊥]Department of Chemistry, Silesian University of Technology, 44-100 Gliwice, Poland

[#]Department of Chemistry, Marquette University, Milwaukee, Wisconsin 53201, United States

Supporting Information

ABSTRACT: Binding of the competitive inhibitor L-captopril to the *dapE*-encoded *N*-succinyl-L,L-diaminopimelic acid desuccinylase from *Neisseria meningitidis* (*Nm*DapE) was examined by kinetic, spectroscopic, and crystallographic methods. L-Captopril, an angiotensin-converting enzyme (ACE) inhibitor, was previously shown to be a potent inhibitor of the DapE from *Haemophilus influenzae* (*Hi*DapE) with an IC_{50} of 3.3 μM and a measured K_i of 1.8 μM and displayed a dose-responsive antibiotic activity toward *Escherichia coli*. L-Captopril is also a competitive inhibitor of *Nm*DapE with a K_i of 2.8 μM. To examine the nature of the interaction of L-captopril with the dinuclear active site of DapE, we have obtained electron paramagnetic resonance (EPR) and magnetic circular dichroism (MCD) data for the enzymatically hyperactive Co(II)-substituted forms of both *Hi*DapE and *Nm*DapE. EPR and MCD data indicate that the two Co(II) ions in DapE are antiferromagnetically coupled, yielding an $S = 0$ ground state, and suggest a thiolate bridge between the two metal ions. Verification of a thiolate-bridged dinuclear complex was obtained by determining the three-dimensional X-ray crystal structure of *Nm*DapE in complex with L-captopril at 1.8 Å resolution. Combination of these data provides new insights into binding of L-captopril to the active site of DapE enzymes as well as important inhibitor−active site residue interaction's. Such information is critical for the design of new, potent inhibitors of DapE enzymes.

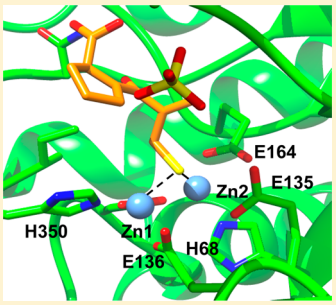

Several pathogenic bacteria, some of which were thought to have been eradicated, have made a significant resurgence because of bacterial resistance to antibiotics.[1,2] According to the Centers for Disease Control and Prevention, several bacterial strains currently exhibit multidrug resistance, with >60% of hospital-acquired infections in the United States caused by the so-called ESKAPE pathogens (*Enterococcus faecium*, *Staphylococcus aureus*, *Klebsiella pneumoniae*, *Acinetobacter baumannii*, *Pseudomonas aeruginosa*, and *Enterobacter* species).[3] To alleviate the problem of antibiotic resistance, it is important that new enzymatic targets be identified and specific inhibitors developed.[4] The *meso*-diaminopimelate (*m*DAP)/lysine biosynthetic pathway offers several potential antibacterial enzyme targets, such as the *dapE*-encoded *N*-succinyl-L,L-diaminopimelic acid desuccinylase (DapE).[5−7] The products of this pathway, mDAP and lysine, are essential components of the peptidoglycan cell wall for Gram-negative and most Gram-positive bacteria, providing a link between polysaccharide strands.[6,8,9] DapE genes have been identified in a large number of pathogenic Gram-positive and Gram-negative bacteria, including all of the ESKAPE pathogens.[10−16] Sequence alignment of these DapE genes reveals a minimum of 49% sequence identity. Deletion of the gene encoding DapE is lethal to *Helicobacter pylori* and *Mycobacterium smegmatis* even in the presence of lysine-supplemented media.[10,17] Therefore, DapEs are essential for bacterial cell growth and, as there are no similar biosynthetic pathways in mammals, are targets for inhibitors that may possess antimicrobial activity.[5]

DapEs are metalloenzymes that catalyze the hydrolysis of *N*-succinyl-L,L-diaminopimelic acid (SDAP), forming L,L-diaminopimelic acid and succinate.[8] DapEs have been purified from multiple sources, but the best characterized example is the DapE from *Haemophilus influenzae* (*Hi*DapE), which is a

Received: April 29, 2015
Revised: July 8, 2015
Published: July 17, 2015

DOI: 10.1021/acs.biochem.5b00475
Biochemistry 2015, 54, 4834−4844

homodimeric enzyme (subunit M_r = 41.6 kDa) that requires two Zn(II) ions per mole of polypeptide for full enzymatic activity.[13] The X-ray crystal structures for both mono- and dinuclear Zn(II) forms of *Hi*DapE [Zn_(*Hi*DapE) and ZnZn(*Hi*DapE)] have been reported previously.[16] In the dinuclear Zn(II) form, each Zn(II) ion adopts a distorted tetrahedral geometry coordinated by one imidazole (H67 for Zn_1 and H349 for Zn_2) and one carboxylate group (E163 for Zn_1 and E135 for Zn_2). Both Zn(II) ions are bridged by an additional carboxylate group (D100) and a water/hydroxide, forming a (μ-aquo)(μ-carboxylato)dizinc(II) core with a 3.3 Å Zn−Zn distance.[16] To date, no X-ray crystallographic data for a DapE−inhibitor complex have been reported.

Thiols are commonly used as inhibitors of Zn(II) metalloproteins because Zn(II) is a relatively soft acid and thiols are soft bases.[18] Examination of several thiol-based compounds led to the identification of moderately strong inhibitors of *Hi*DapE.[14,19] For example, L-penicillamine exhibits an IC_{50} value of 13.7 μM toward *Hi*DapE and is a competitive inhibitor with a measured K_i of 4.6 μM. DapE is also stereoselective with respect to the recognition of substrate and inhibitors, as D-penicillamine provided an IC_{50} value of 50 μM.[14] Similarly, L-captopril, an angiotensin-converting enzyme (ACE) inhibitor, exhibited an IC_{50} value of 3.3 μM toward *Hi*DapE, while D-captopril yielded an IC_{50} value of 42 μM. L-Captopril was shown to be a competitive inhibitor of *Hi*DapE with a measured K_i of 1.8 μM and displayed a dose-responsive antibiotic activity toward *Escherichia coli*.[14] Even though L-captopril is a moderately tight binding inhibitor of DapE enzymes and is a promising lead compound for the development of a novel class of DapE inhibitors, no information about how L-captopril binds to DapE, a requirement for the rational design of new, more potent DapE inhibitors, has been published.

A likely important characteristic of a highly specific, tight binding inhibitor of DapE enzymes will be the molecule's ability to bind to the metal ions in the active site. Several factors are important for interactions of L-captopril with the active site metal ions of DapE, some of which are metal coordination geometry, open metal coordination sites (i.e., those filled by water molecules), and the number of active site metal ions. Therefore, we have analyzed the binding of L-captopril to *Hi*DapE and the DapE from *Neisseria meningitidis* (*Nm*DapE) via kinetic and spectroscopic methods. We have also determined the X-ray crystal structure of the *Nm*DapE enzyme in complex with L-captopril at 1.8 Å resolution. These data provide insight into interactions of L-captopril with the active site metal ions as well as adjacent active site amino acid residues, providing new insight into the rational design of new, more potent inhibitors of DapE enzymes.

METHODS

Materials. D,L-α,ε-Diaminopimelic acid (98%), succinic anhydride, and ion-exchange resin (Dowex 50WX8-200, H^+ form) were purchased from Sigma. 2-Naphthalenesulfonic acid 1-hydrate (98%) was purchased from TCI, and microcrystalline cellulose was purchased from Merck. All other chemicals were purchased from commercial sources and were of the highest quality available. SDAP was synthesized using the procedure described by Lin et al.,[20] providing an overall yield of 41%.

Cloning, Expression, and Purification of DapE. The *Hi*DapE enzyme was expressed and purified as described previously.[21] The DapE gene from *N. meningitidis* (*Nm*DapE) was cloned into the pMCSG7 vector using the ligation-independent cloning method.[22] The following primers were used: 5′-TAC TTC CAA TCC AAT GCC GCA GCT GCA GCT GCA AAA GAA AAA GTG GTT TCG TTG GCA CAA G-3′ and 5′-TTA TCC ACT TCC AAT GTT AGT TAG CTA TCC AAT AAA TTC ACT AAC ATT TTG TG-3′. The PCR product was purified using the QIAquick PCR Purification Kit (Qiagen) to remove the primers and dNTPs from the PCR mixture. T4 polymerase was employed to create overhangs on the PCR fragments. The resulting plasmid was transformed into BL21(DE3)/magic *E. coli* competent cells and grown in Luria-Bertani broth containing ampicillin (150 μg mL^{-1}) and kanamycin (25 μg mL^{-1}) at 37 °C to an A_{600} of 1.0 while being shaken. IPTG was added (0.4 mM), and culture growth was continued for 16 h at 18 °C. Cells were recovered by centrifugation (12000*g*) for 15 min at 4 °C using a Beckman Coulter Avanti J-E Centrifuge. *Nm*DapE was purified according to the standard protocol for Ni-NTA affinity chromatography, and all steps were performed at 4 °C.[23] The His_6 tag was removed by treating each enzyme with His_6-tagged TEV protease for 16 h at 4 °C in 50 mM HEPES (pH 8.0). Cleaved protein was separated from His_6-tagged TEV using Ni-NTA affinity chromatography.

Enzymatic Assay. The specific activity of *Hi*DapE and *Nm*DapE was determined using a 50/50 mixture of D,D- and L,L-SDAP as the substrate in 50 mM phosphate buffer (PP_i) (pH 7.5) as previously described.[24] The kinetic parameters V_{max} and K_m were determined by quantifying amide bond cleavage (decrease in absorbance) of L,L-SDAP at 225 nm (ε = 698 M^{-1} cm^{-1}) in triplicate using a Shimadzu UV-2450 spectrophotometer equipped with a temperature controller (25 °C). Enzyme activities are expressed as units per milligram, where 1 unit is defined as the amount of enzyme that releases 1 μmol of L,L-SDAP at 30 °C in 1 min. Catalytic activities were determined with an error of ±10%. Initial rates were fit directly to the Michaelis−Menten equation to obtain the catalytic constants K_m and k_{cat} using Origin software.

Inhibition of *Nm*DapE by L-Captopril. The kinetic parameters v (velocity), k_{cat} ($V_{max}/[E]_0$), K_m (Michaelis constant), and K_i (inhibition constant) were determined in 50 mM phosphate buffer (pH 7.5) spectrophotometrically by recording the initial velocity of the hydrolysis of L,L-SDAP at 25 °C in triplicate.[14] L-Captopril concentrations ranged from 0 to 0.1 mM. The linearity of the progress curves for product formation in the absence and presence of an inhibitor indicated that L-captopril is in rapid equilibrium with *Nm*DapE. The initial rates were plotted against substrate concentration, and the kinetic constants were calculated using Origin software.[20,24,25]

Co(II)-Substituted DapE Samples. Apo-DapE was prepared by extensive dialysis for 72 h at 4 °C against 10 mM EDTA in 50 mM HEPES buffer (pH 7.5). DapE was then exhaustively dialyzed against metal-free (Chelex-100 treated) 50 mM HEPES buffer (pH 7.5). Any remaining metal ions were estimated by comparing the activity of the apoenzyme with that of a sample that had been reconstituted with Zn(II). DapE incubated with EDTA typically had <5% residual activity after dialysis. The mono- and dicobalt(II) forms of *Hi*DapE and *Nm*DapE were prepared using apo-DapE samples that were incubated with $CoCl_2$ (99.999%; Strem Chemicals, Newburyport, MA) for 30 min at 25 °C prior to exhaustive dialysis into Chelex-100-treated buffer as previously reported.[26]

DOI: 10.1021/acs.biochem.5b00475
Biochemistry 2015, 54, 4834−4844

Electron Paramagnetic Resonance Spectroscopy. Electron paramagnetic resonance (EPR) spectra were recorded at 4.5−35 K and 9.63 GHz (ER4116DM resonator with $\mathbf{B}_0 \perp \mathbf{B}_1$), 9.37 GHz (ER4116DM resonator with $\mathbf{B}_0 \| \mathbf{B}_1$), or 9.39 GHz (SHQ resonator) using 1.2 mT (12 G) magnetic-field modulation at 100 kHz with phase-sensitive detection on a Bruker EleXsys E600 spectrometer equipped with an Oxford Instruments ESR900 helium flow cryostat and ITC503 temperature controller. The SHQ resonator has a $\mathbf{B}_1$ for a given microwave power significantly higher than that of the ER4116DM resonator (we estimate by a factor of ∼5). Background signals were collected on samples of frozen buffer and subtracted.

Magnetic Circular Dichroism Studies. The magnetic circular dichroism (MCD) instrument consists of a JASCO J815 spectropolarimeter and an Oxford Instruments SM4000 cryostat/magnet. Variable-temperature variable-field (VTVH) MCD data were collected in increments of 0.5 T (T) from 0 to 7.0 T and at temperatures (nominally) of 1.5, 3.0, 6.0, 12, 24, and 48 K. Spectra were collected at a 1.0 nm bandwidth and scanned at 50 nm/min using a time constant of 1 s. The sample cell has a 0.62 cm path length. Each spectrum was corrected for any natural CD by subtracting the zero-field spectrum of the sample. Even when there is no sample present, the instrument baseline exhibits a small deviation from zero that is both field- and wavelength-dependent. Therefore, each spectrum was also corrected by subtraction of a spectrum recorded at the same magnetic field but with no sample present. The MCD spectra were fit to the minimal number of Gaussian peaks using Grams AI 9.1 after converting the spectra to wavenumber units. In the fitting process, a minimal number of Gaussians were fit to achieve a satisfactory composite spectrum. Fitting of the VTVH MCD data was achieved using a Fortran program, VTVH 2.1.1, written by M. Riley.[27] The spin Hamiltonian and additional details of the fitting program have been described previously.[28] The fits were tested for robustness once a complete set of parameters had been obtained. To do this, the initial parameters were set to the best-fit parameters and then all allowed to float. Subsequently, one key parameter such as J, D, M_{xy}, M_{xz}, or M_{yz} was chosen, and its initial value was set differently, after which the fit process was repeated. Percent polarization for a given fit was calculated from M_{xy}, M_{yz}, and M_{xz} using $\%M_x = (M_{xy} \times M_{yz})^2/[(M_{xy} \times M_{xz})^2 + (M_{xy} \times M_{yz})^2 + (M_{xz} \times M_{yz})^2]$. M_y and M_z were calculated correspondingly.[29] Finally, the VTVH MCD data fitting program used a spin Hamiltonian that included the term $H = -2JS_1S_2$.

Protein Crystallization. Prior to crystallization, a 25 mg/mL *Nm*DapE protein sample was incubated with 3 equiv of Zn(II) ions and left on ice for 20 min to equilibrate. Zinc(II)-loaded *Nm*DapE was screened against 300 commercially available conditions (Index HT and PEG/Ion HT from Hampton Research and Wizard TM from Emerald Biosystems) using a Mosquito liquid handling robot with 96 plates.[30] Several crystallization conditions were characterized yielding diffraction quality crystals. All crystals were screened, and data were collected on the best-diffracting crystals, which were grown by the sitting-drop vapor-diffusion method at 16 °C using 400 nL of a precipitant solution [20% (w/v) PEG 3350 and 100 mM HEPES (pH 7.5)] and 400 nL of [ZnZn(*Nm*DapE)]. X-ray quality crystals appeared within 2 weeks. Crystals of [Zn_*Nm*DapE] were also crystallized by the sitting-drop vapor-diffusion method at 16 °C but with a 400 nL precipitant solution [15% (w/v) PEG 3350 and 100 mM succinic acid (pH 7.0)] and 400 nL of a protein, providing crystals within 2 weeks. Crystals of [ZnZn(*Nm*DapE)] in complex with L-captopril were obtained by mixing 400 nL of a precipitant solution [0.2 M ammonium acetate, 0.1 M TRIS (pH 8.5), and 25% (w/v) polyethylene glycol 3350] in a 1:1 ratio with a solution of [ZnZn(*Nm*DapE)] incubated with a 30 mM solution of L-captopril [50 mM HEPES (pH 7.5) and 150 mM NaCl] with crystals appearing within 3 weeks.

Structure Solutions and Refinement. The X-ray data were collected at beamline 19-ID of the Structural Biology Center at the Advanced Photon Source.[31] All data were processed and scaled using HKL3000.[32] Molecular replacement searches were completed with MOLREP within the CCP4 suite using the structure of apo-*Nm*DapE as a template [Protein Data Bank (PDB) entry 1VGY].[16] The asymmetric unit of [Zn_(*Nm*DapE)] (space group $P2_12_12_1$) contains a dimer, while crystals of [ZnZn(*Nm*DapE)] and [ZnZn(*Nm*DapE)] in complex with L-captopril both crystallized in the $C222_1$ space group and contained only one subunit of the dimer in the asymmetric unit. Several rounds of rebuilding and readjusting using COOT[33] and refinement using REFMAC[34] and PHENIX[35] improved the initial models. The final models were refined against 95% of the reflections within the resolution ranges. The remaining 5% of the reflections, which were randomly selected, were used to monitor R_{free}. The final refinement statistics are listed in Table 1. Analysis and validation of all structures were performed with the aid of PROCHECK[36] and MOLPROBITY.[37] The refinement restraints for the L-captopril structure were created with the assistance of COOT and were generated from SMILE string.[38]

PDB Coordinates. The atomic coordinates for [Zn_(*Nm*DapE)], [ZnZn(*Nm*DapE)], and [ZnZn(*Nm*DapE)] bound by L-captopril were deposited in the PDB as entries 4O23, 4PPZ, and 4PQA, respectively.

RESULTS

Kinetic Studies of [Zn_(*Nm*DapE)] and [ZnZn-(*Nm*DapE)]. Steady-state kinetic parameters for the hydrolysis of L,L-SDAP by [Zn_(*Nm*DapE)] and [ZnZn(*Nm*DapE)] and [Zn_(*Hi*DapE)] and [ZnZn(*Hi*DapE)] are listed in Table 2. The kinetic parameters obtained for Zn(II)-loaded *Nm*DapE are very similar to those previously reported for Zn(II)-loaded *Hi*DapE.[14] Of note is the lack of dependence of K_m on the zinc content, while the dizinc forms exhibit almost twice the catalytic efficiency of the monozinc forms. L-Captopril was found to be a competitive inhibitor of [ZnZn(*Nm*DapE)] with a K_i of 2.8 μM, a value similar to that observed for [ZnZn(*Hi*DapE)] (K_i of 1.8 μM).

EPR Spectra of L-Captopril Bound to [Co_(*Nm*DapE)], [CoCo(*Nm*DapE)], [Co_(*Hi*DapE)], and [CoCo(*Hi*DapE)]. EPR spectra of the resting forms of Co(II)-substituted *Nm*DapE (Figure 1A) and *Hi*DapE (Figure 1B) reveal clear similarities. At 13 K and a nonsaturating microwave power, the [Co_(DapE)] spectra (traces A in panels A and B of Figure 1) are complex and appear to be due to a moderately rhombic ($E/D \leq 0.15$) $M_S = \pm^1/_2$ signal with resonances at $g' = 5.35$ (1250 G), 4.05 (1660 G), and 2.25 (3015 G), superimposed on an $M_S = \pm^3/_2$ signal with a sharp resonance at $g' = 6.5$ (1030 G) and a broad derivative feature with an estimated turning point at $g' \approx 1.15$. At 4.5 K and a high microwave power (traces B in panels A and B of Figure 1), the $M_S = \pm^1/_2$ signals are almost completely extinguished. This latter behavior indicates that the $M_S = \pm^1/_2$ signals are due to thermal population of the $M_S =$

DOI: 10.1021/acs.biochem.5b00475
Biochemistry 2015, 54, 4834−4844

Table 1. Data and Refinement Statistics

	[Zn_*Nm*DapE]	[ZnZn_*Nm*DapE]	[ZnZn_*Nm*DapE]-L-captopril
	Data Collection		
space group	$P2_12_12_1$	$C222_1$	$C222_1$
unit cell (Å)	a = 55.3	a = 117	a = 116.9
	b = 111.4	b = 151.6	b = 151.5
	c = 132.5	c = 55.5	c = 55.1
resolution (Å)	39.2−2.09	29.4−2.0	27.5−1.78
wavelength (Å)	0.98	0.98	0.98
no. of observed reflections	204709	202836	178375
no. of unique reflections	48738	33502	46112
redundancy[b]	4.2 (4.0)	6.1 (5.8)	3.9 (3.8)
R_{merge}[a,b] (%)	7.4 (82.1)	8.5 (89.9)	6.5 (75.2)
R_{pim}[a,b] (%)	4.0 (45.7)	4.3 (59.4)	3.3 (44.2)
completeness[b] (%)	99.1 (96.7)	100 (100)	97.7 (99.5)
I/σ	17.9 (1.5)	22.8 (1.9)	17.7 (1.7)
phasing			
phasing method	MR	MR	MR
	Refinement		
R_{cryst} (%)	21.3	17.5	16.4
R_{free} (%)	24.1	20.8	19.6
no. of protein residues	746	374	374
no. of zinc/phosphate/sulfate ions	3/−/4	2/1/−	2/-/1
no. of solvent molecules	380	237	284
rmsd from target values			
bond lengths (Å)	0.003	0.020	0.021
bond angles (deg)	0.71	1.69	1.90
average B factor (Å^2)			
protein	43.8	32.2	24.8
Zn	32.0	23.2	17.9
H_2O	37.8	24.19	34.6
PDB entry	4O23	4PPZ	4PQA
Ramachandran (%)[c] MF/AA	97.4/2.6	97.6/2/4	97.9/2.1

[a] $R_{merge} = \sum_{hkl}\sum_i|I_{i(hkl)} - \langle I_{hkl}\rangle|/\sum_{hkl}\sum_i I_{i(hkl)}$, where $I_{i(hkl)}$ is the ith observation of reflection hkl and $\langle I_{hkl}\rangle$ is the weighted average intensity for all observations i of reflection hkl. $R_{pim} = \sum_{hkl}[1/(N-1)^{1/2}]\sum_i|I_{i(hkl)} - \overline{I}_{hkl}|/\sum_{hkl}\sum_i I_{i(hkl)}$. [b] Numbers in parentheses are values for the highest-resolution bin. [c] As defined by MOLPROBITY (MF, most favored, AA, additionally allowed).

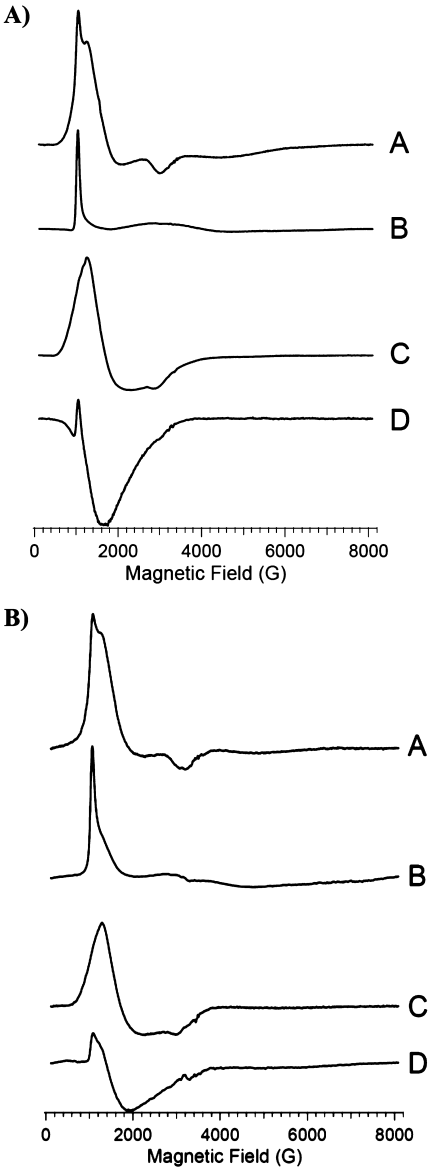

Figure 1. (A) EPR spectra at 9.39 GHz (SHQ resonator) of [Co_(*Nm*DapE)] (A and B) and [CoCo(*Nm*DapE)] (C and D), recorded at 13 K and 0.5 mW (A and C) and 4.5 K and 100 mW (B and D). Spectral amplitudes are shown normalized for $1/T$, $(P_{microwave})^{1/2}$, and the number of equivalents of Co(II) added. (B) EPR spectra at 9.39 GHz (SHQ resonator) of [Co_(*Hi*DapE)] (A and B) and [CoCo(*Hi*DapE)] (C and D), recorded at 13 K and 1.0 mW (A and C) and 4.5 K and 200 mW (B and D). Spectral amplitudes are shown normalized for $1/T$, $(P_{microwave})^{1/2}$, and the number of equivalents of Co(II) added.

$\pm^1/_2$ Kramers' doublet at a higher temperature associated with an excited state with a zero-field splitting, Δ, on the order of 10 cm^{-1} for [Co_(*Nm*DapE)], and less for [Co_(*Hi*DapE)], where some $M_S = \pm^1/_2$ contribution is still evident at 4.5 K (1 cm^{-1} corresponds to 1.44 K). If the $M_S = \pm^1/_2$ signals were

Table 2. Kinetic Constants for [Zn_(DapE)] and [ZnZn(DapE)] from *N. meningitidis* and *H. influenzae*

	*Nm*DapE		*Hi*DapE	
	Zn	ZnZn	Zn	ZnZn
K_m (μM)	795 ± 20	610 ± 11	730 ± 15	730 ± 15
k_{cat} (s^{-1})	76 ± 10	120 ± 10	80 ± 5	140 ± 10
k_{cat}/K_m (mM^{-1} min^{-1})	5700 ± 200	11800 ± 200	6600 ± 200	11400 ± 200

DOI: 10.1021/acs.biochem.5b00475
Biochemistry 2015, 54, 4834−4844

ground-state signals due to a distinct chemical species, rapid-passage signals would be expected rather than disappearance or diminution of the signals.[39] These data indicate a preferred binding site with an $M_S = \pm^3/_2$ ground state, suggesting a distorted tetrahedral coordination environment.[39]

Upon addition of a second equivalent of Co(II), a poorly resolved and apparent $M_S = \pm^1/_2$ signal was observed at 13 K (traces C in panels A and B of Figure 1). In addition, a very weak but clearly identifiable ^{59}Co hyperfine pattern with A_z = 90 G was observed on the low-field edge of the $M_S = \pm^1/_2$ signal, centered at $g' = 7.9$ (850 G; see, e.g., Figure 1A, trace C), but is not clearly visible at the scale used in panels A and B of Figure 1. This hyperfine signal could be due to a small amount of an additional $M_S = \pm^3/_2$ signal with $g_{real(z)} \sim 2.6$ or else a very rhombic ($E/D \sim {}^1/_3$) $M_S = \pm^1/_2$ signal with $g_{real(y)} \sim 2.9$; the origin of the hyperfine split signal is unclear, but it was completely insensitive to L-captopril and was not considered further.

In contrast to the case for [Co_(*Nm*DapE)] and [Co_(*Hi*DapE)], when EPR spectra of [CoCo(*Nm*DapE)] and [CoCo(*Hi*DapE)] were recorded at 4.5 K, the predominant $M_S = \pm^1/_2$ signal was clearly still observable as a rapid-passage signal that appeared as an inverted absorption-shaped feature, superimposed on the sharp $M_S = \pm^3/_2$ signal at $g' = 6.5$ (traces D in panels A and B of Figure 1). The appearance of a slowly relaxing ground-state $M_S = \pm^1/_2$ signal is consistent with the second added equivalent of Co(II) occupying a five- or six-coordinate site. There is a slight difference between the signals from [CoCo(*Nm*DapE)] and [CoCo(*Hi*DapE)]. The signal from [CoCo(*Nm*DapE)] appears to account for the entire complement of Co(II), whereas that from [CoCo(*Hi*DapE)] indicates that some EPR silent Co(II) is present. Further, the $M_S = \pm^3/_2$ signal in [CoCo(*Hi*DapE)] is significantly smaller than in [Co_(*Hi*DapE)] (traces D and B, respectively, in Figure 1B), whereas this is not the case in [CoCo(*Nm*DapE)] (traces D and B, respectively, in Figure 1A; note that in both panels A and B of Figure 1, traces D have been multiplied by 0.5 relative to traces B to account for 2 vs 1 equiv of Co^{2+}). These data suggest a weak antiferromagnetic interaction between the Co(II) ions in [CoCo(*Hi*DapE)], such that $|J| > h\nu$ for some, but not all, of the population of dinuclear centers in the sample, i.e., that there is a distribution of J that includes 0.3 cm^{-1}. No parallel mode ($\mathbf{B}_0 \| \mathbf{B}_1$) EPR signals were observed.

Addition of L-captopril induced differential effects in [CoCo(*Nm*DapE)] and [CoCo(*Hi*DapE)]. Addition of L-captopril to [CoCo(*Nm*DapE)] resulted in the sharp $M_S = \pm^3/_2$ signal at $g' = 6.5$ being essentially extinguished, but no overall signal intensity was lost (Figure 2, traces A and B). This is consistent with additional coordination to the hitherto four-coordinate Co(II) ion but no mediation of significant (≥0.3 cm^{-1}) exchange coupling between the two Co(II) ions. In contrast, the addition of L-captopril to [CoCo(*Hi*DapE)] leads to a wholesale loss of ~30% of the EPR intensity, with no detectable change in line shape (Figure 2, traces C and D), signifying an increase, albeit modest, in the level of exchange coupling between the two Co(II) ions.

MCD Spectra of L-Captopril Bound to [Co_(*Nm*DapE)], [CoCo(*Nm*DapE)], [Co_(*Hi*DapE)], and [CoCo(*Hi*DapE)]. MCD spectra of [CoCo(*Nm*DapE)] and [CoCo(*Hi*DapE)] are nearly identical in shape, band energy, and intensity (Figure 3). It should be noted that the MCD spectra obtained at ambient temperature in the absence of a glycerol glassing agent have the same bands as the low-temperature spectra; however, they are much less intense and broader. All of the bands display temperature-dependent C-terms arising from the paramagnetic high-spin Co(II) ground states. The intense negative band at 576 nm is asymmetric because of a small component at 559 nm in [CoCo(*Hi*DapE)] and at 558 nm in [CoCo(*Nm*DapE)]. This intense negative band along with an intense positive band at 532 nm is characteristic of high-spin Co(II) in a distorted tetrahedral ligand field.[40−42] These bands arise from the $^4A_2 \rightarrow {}^4T_1(P)$ d−d transition in T_d that has been split into three components by the lowe-symmetry environment in the active site. The negative band at 503 nm along with a very weak positive band at shorter wavelengths is characteristic of high-spin Co(II) in a distorted octahedral ligand field.[40,41,43,44] The band at 503 nm arises from the $^4T_{1g} \rightarrow {}^4T_{1g}(P)$ d−d transition in O_h that can broaden or split at lower symmetries. The 503 nm band does not split in [CoCo(*Nm*DapE)] or [CoCo(*Hi*DapE)] but is noticeably broader in [CoCo(*Hi*DapE)] than in [CoCo(*Nm*DapE)]. The very weak positive bands at 463 and 475 nm in [CoCo(*Hi*DapE)] and [CoCo(*Nm*DapE)], respectively, are doublet transitions, which gain intensity through spin−orbit coupling to the nearby spin-allowed 503 nm band.[43] Despite the similarity in the MCD spectra of [CoCo(*Hi*DapE)] and [CoCo(*Nm*DapE)], there is a difference in the relative metal binding affinities between the two enzymes. When 1 equiv of Co(II) is added to apo-*Nm*DapE, both the six-coordinate and four-coordinate sites are partially occupied (Figure SI-1 of the Supporting Information). Addition of a second equivalent of Co(II) saturates both binding sites. On the other hand, addition of 1 equiv of Co(II) to apo-*Hi*DapE saturates the four-coordinate site, leaving the six-coordinate site virtually empty (Figure SI-2 of the Supporting Information).

VTVH MCD data were collected at 503, 532, and 576 nm on both [CoCo(*Nm*DapE)] and [CoCo(*Hi*DapE)]. These data were used to construct magnetization plots; typical examples are shown in Figures SI-3−SI-8 of the Supporting Information. The VTVH MCD data were fit as previously described,[27] which yielded the electronic ground-state parameters for magnetic exchange coupling (J) and axial (D) and rhombic (E) zero-field splitting (ZFS). Typical fits are also shown in Figures SI-3−SI-8 of the Supporting Information. Multiple experiments were run,

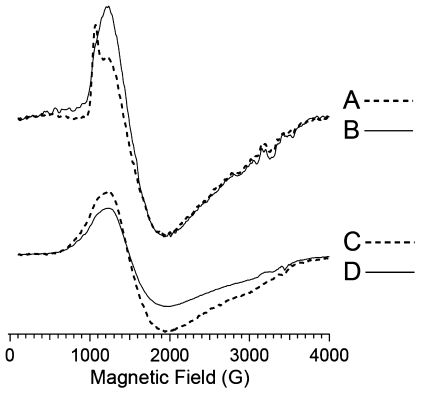

Figure 2. EPR spectra at 9.63 GHz (ER4116DM resonator) of [CoCo(*Nm*DapE)] before (A) and after (B) the addition of L-captopril and [CoCo(*Hi*DapE)] before (C) and after (D) the addition of L-captopril. Spectra were recorded at 4.5 K and 100 mW. Spectral amplitudes are shown normalized for $1/T$, $(P_{microwave})^{1/2}$, and the number of equivalents of Co(II) added.

DOI: 10.1021/acs.biochem.5b00475
Biochemistry 2015, 54, 4834−4844

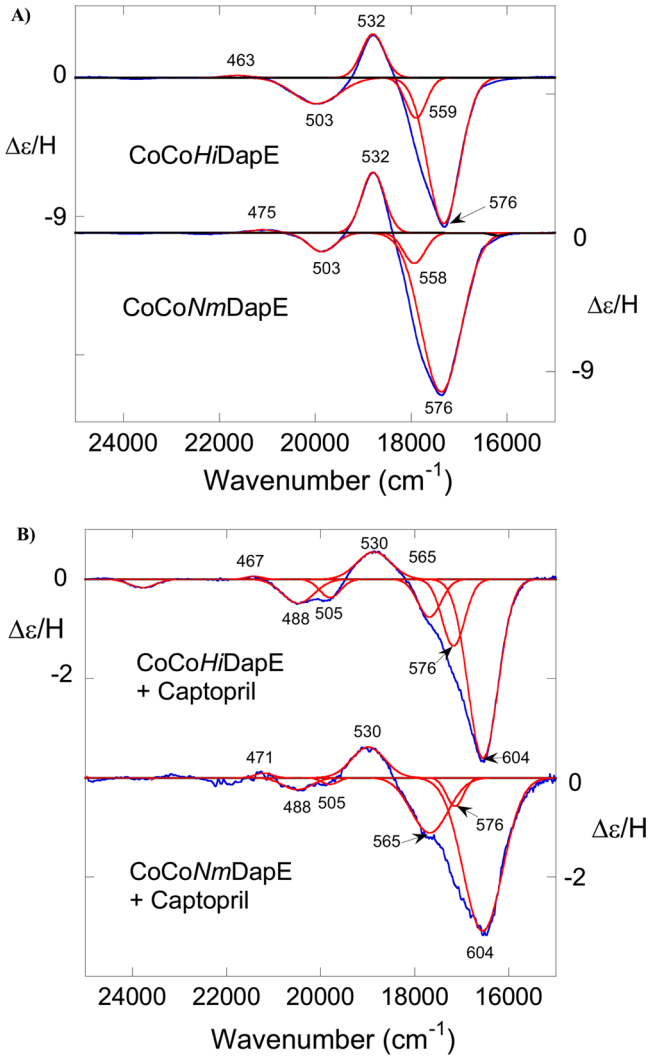

Figure 3. MCD spectra of (A) [CoCo(*Hi*DapE)] (top) and [CoCo(*Nm*DapE)] (bottom) and (B) [CoCo(*Hi*DapE)] with 5 equiv of L-captopril (top) and [CoCo(*Nm*DapE)] with 5 equiv of L-captopril (bottom). All spectra were recorded at 1.3 K and 7.0 T in a 0.62 cm path length cell. The enzymes were in a 60/40 (v/v) glycerol/buffer solution. [CoCo(*Hi*DapE)] at 32 mg/mL [0.77 mM enzyme, 1.6 mM in active sites, 3.1 mM in Co(II)]. [CoCo(*Nm*DapE)] at 29 mg/mL [0.70 mM enzyme, 1.4 mM in active sites, 2.8 mM in Co(II)]. The units of $\Delta\varepsilon/H$ are M^{-1} cm^{-1} T^{-1}, where the concentration of active sites was used. In both panels, the blue trace is the experimental spectrum and the red traces are the Gaussians used to fit the spectra.

and average values of these parameters along with the standard deviations are given in Table 3. Magnetic exchange coupling, if it occurs, will be strongest through monatomic bridges (e.g., μ-1,1 as opposed to μ-1,3). In none of the fittings of the VTVH data from [CoCo(*Nm*DapE)] or [CoCo(*Hi*DapE)] was the quality of the fit improved (lower value of χ^2) by having a non-zero J (positive or negative). This strongly suggests that the bridging oxygen atom is in the form of a μ-aqua as opposed to a μ-hydroxo. Many dicobalt(II) complexes with either a μ-aqua or μ-hydroxo have been studied.[8,44−46] Aqua-bridged complexes consistently exhibit a small antiferromagnetic coupling (negative J) or no coupling at all, whereas hydroxo-bridged complexes consistently have a small ferromagnetic (positive J) coupling. In addition to the previously reported dicobalt(II) complexes, three new model complexes that are consistent with this trend are shown in Figures SI-13 and SI-14 of the Supporting Information. The ZFS parameters that were determined in the fitting of the VTVH data from [CoCo(*Nm*DapE)] and [CoCo(*Hi*DapE)] were also consistent with assignment of the 503 nm band to a six-coordinate Co(II), and the 532 and 576 nm bands to a distorted four-coordinate Co(II). Generally, the axial ZFS parameter, D, is >50 cm^{-1} for six-coordinate high-spin Co(II) and <10 cm^{-1} for four-coordinate high-spin Co(II).[8,42]

The addition of 1 equiv (based on the concentration of active sites) of L-captopril to either [CoCo(*Hi*DapE)] or [CoCo(*Nm*DapE)] has no apparent effect on the MCD spectra. However, addition of 5 equiv of L-captopril causes the green resting enzyme solutions to turn blue (Figure 3B). The four-coordinate Co(II) bands shift from 532, 559, and 576 nm in [CoCo(*Hi*DapE)] to 530, 565, and 604 nm, respectively, in the [CoCo(*Hi*DapE)]−L-captopril complex, while the bands for the same species shift from 532, 558, and 576 nm in [CoCo(*Nm*DapE)] to 530, 565, and 604 nm, respectively, in the [CoCo*Nm*DapE]−L-captopril complex. The six-coordinate band at 503 nm splits into two bands at 488 and 505 nm for the [CoCo(*Hi*DapE)]−L-captopril and [CoCo(*Nm*DapE)]−L-captopril complexes. There is a small peak at 576 nm in both spectra, which is due to uncomplexed enzyme. In addition to these band shifts, there is a roughly 3-fold decrease in MCD intensity, which is not due to loss of Co(II) from the enzyme caused by L-captopril. Finally, the quality of the optical glasses formed in the presence of L-captopril is not as high as for the resting enzyme alone. The resulting MCD spectra had signal-to-noise ratios considerably lower than those of the MCD spectra obtained for the resting enzymes.

VTVH MCD data were also collected on the 505, 530, and 604 nm bands in the [CoCo(*Hi*DapE)]−L-captopril complex

Table 3. VTVH MCD Fitting Parameters

parameter	[CoCo(*Nm*DapE)][a]	[CoCo(*Nm*DapE)] and captopril[b]	[CoCo(*Hi*DapE)][c]	[CoCo(*Hi*DapE)] and captopril[d]
J (cm^{-1})	0	−0.1	0	−0.05 ± 0.04
D (cm^{-1}), 4C	3.7 ± 0.6	0.05	3.7 ± 1.0	4.1 ± 1.5
E/D, 4C	∼0	0.002	∼0	0.25 ± 0.14
D (cm^{-1}), 6C	>100	>50	>100	28 ± 5
E/D, 6C	0.18 ± 0.04	∼0	0.27 ± 0.04	0.08 ± 0.03
polarization	503 nm *x*-pol.	505 nm na	503 nm *x*-pol.	505 nm *z*-pol.
	532 nm *xy*-pol.	530 nm na	532 nm *xy*-pol.	530 nm *z*-pol.
	576 nm *xy*-pol.	604 nm *z*-pol.	576 nm *xy*-pol.	604 nm *z*-pol.

[a]Based on three independent experiments; ±one standard deviation. [b]Based on a single experiment. [c]Based on eight independent experiments. [d]Based on four independent experiments.

DOI: 10.1021/acs.biochem.5b00475
Biochemistry 2015, 54, 4834−4844

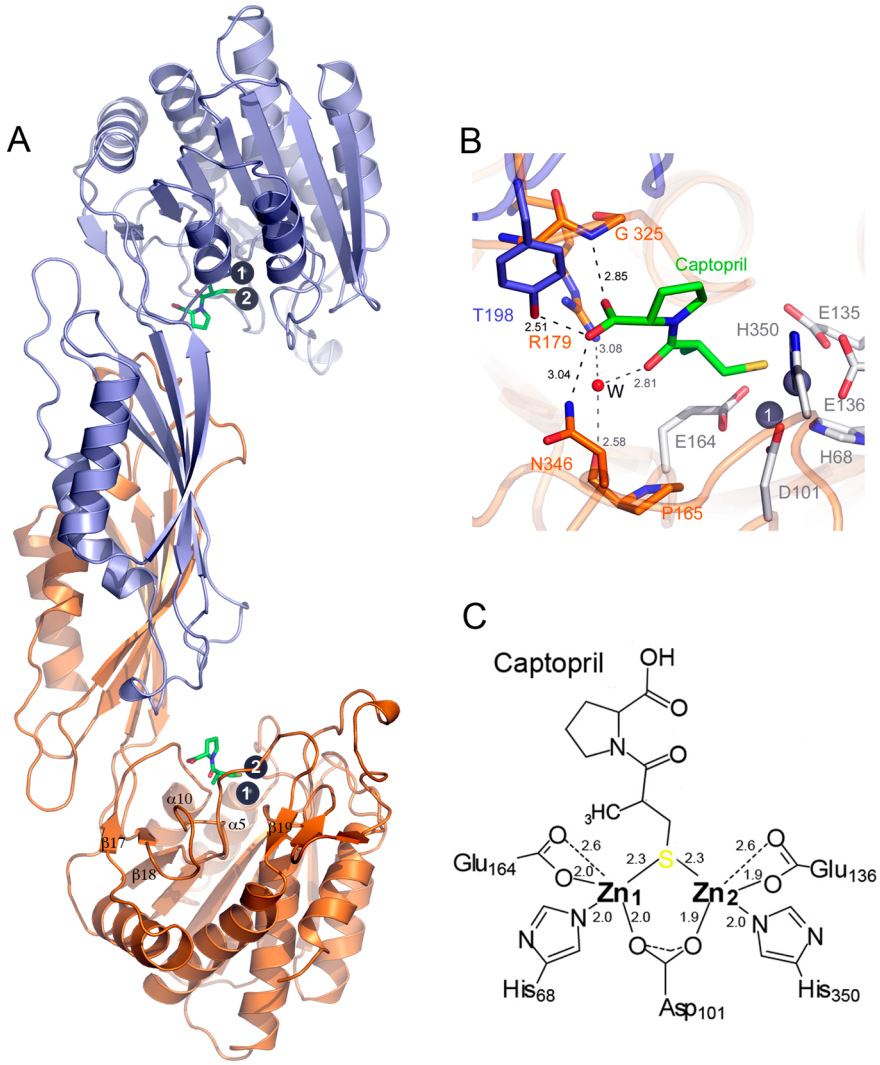

Figure 4. Structure of the [ZnZn(*Nm*DapE)]−L-captopril complex. (A) Ribbon diagram of the homodimer of [ZnZn(*Nm*DapE)] (subunit A colored orange and subunit B blue). The Zn(II) ions in the dinuclear active site are shown as black spheres, while molecules of L-captopril are shown as green sticks. (B) Close-up of the active site region showing the hydrogen bonding interactions of L-captopril (green) with surrounding protein residues and solvent molecule (red sphere). The active site residues are color-coded (orange and blue sticks) according to the subunit coloring, while the conserved residues binding to the Zn(II) ions are colored gray. (C) Schematic drawing of the dinuclear Zn(II) active site bound by L-captopril (distances in angstroms).

and only for the 604 nm band in the [CoCo(*Nm*DapE)]−L-captopril complex. Example magnetization plots and fits are shown in Figures SI-9−SI-12 of the Supporting Information. The χ^2 values for fits of the 505 and 530 nm data are quite high as is the χ^2 value for the 604 nm data for the [CoCo(*Nm*DapE)]−L-captopril complex. The best fits were obtained with a small negative value for *J*. In addition, the ZFS parameters for both the six- and four-coordinate sites changed but were still in the ranges expected for the corresponding Co(II) species (Table 3).

Crystal Structures of [Zn_(*Nm*DapE)], [ZnZn(*Nm*DapE)], and the L-Captopril-Bound [ZnZn(*Nm*DapE)] Complex. The X-ray crystal structures of [Zn_(*Nm*DapE)] (2.1 Å), [ZnZn(*Nm*DapE)] (2.0 Å), and the [ZnZn(*Nm*DapE)]−L-captopril complex (1.8 Å) were determined. These three structures along with that of apo-*Nm*DapE, which was previously determined (PDB entry 1VGY),[47] reveal the typical two-domain homodimer structure (either present in the asymmetric unit or generated by the crystallographic 2-fold axis) observed for all DapE enzymes. Comparison of all four structures of *Nm*DapE shows that the overall fold is well-preserved and the structures of the apo, monozinc, dizinc, and L-captopril-bound forms are nearly identical. Each of these structures overlays with an rmsd for Cα atoms of 0.59 Å {apo-*Nm*DapE over [Zn_(*Nm*DapE)]} and 0.73 Å {apo-*Nm*DapE over [ZnZn(*Nm*DapE)] and L-captopril-bound [ZnZn(*Nm*DapE)]}. Close analysis of the [ZnZn(*Nm*DapE)] and [ZnZn(*Nm*DapE)]−L-captopril structures [both were determined from isomorphous crystals grown under similar conditions (Table 1)] reveals that inhibitor binding does not introduce any significant changes into the structure as evidenced by a very low rmsd of 0.2 Å. Furthermore, examination of the active site regions of the [ZnZn(*Nm*DapE)] structure indicates that the metal ions and ligands are in nearly identical positions. The dinuclear Zn(II) active sites in both [ZnZn(*Nm*DapE)] and the [ZnZn(*Nm*DapE)]−L-captopril complex adopt coordination geometries identical to that reported for *Hi*DapE.[16]

DOI: 10.1021/acs.biochem.5b00475
Biochemistry 2015, 54, 4834−4844

For [ZnZn(*Nm*DapE)], the first metal binding site, Zn_1, resides in a distorted tetrahedral geometry and is bound by the carboxylate OD1 atom of D101 and OE1 atom of E164 as well as the NE1 atom of H68. The Zn_2 metal ion resides in a distorted trigonal bipyramidal geometry and is bound by the NE2 atom of H350, two oxygen atoms, OD2 from D101 and OE2 from E136, and the O1 atom of ethylene glycol. Interestingly, for [Zn_(*Nm*DapE)] a full dimer resides in the asymmetric unit, and Zn(II) binding is different between the two active sites. In one of the active sites, a single Zn(II) ion is bound in the first metal binding site, while in the second active site, two Zn(II) ions are present but with occupancies modeled at 60% for Zn_1 and 18% for Zn_2. These data suggest that metal binding is not strictly sequential for *Nm*DapE, which is different from that observed for *Hi*DapE.

The 1.8 Å structure of the [ZnZn(*Nm*DapE)]−L-captopril complex reveals clear electron density corresponding to L-captopril inside the positively charged groove, formed between the catalytic and dimerization domains (Figure 4). The sulfhydryl group of L-captopril bridges the two active site Zn(II) ions with Zn−S distances of 2.3 Å, displacing the bridging water molecule. The carboxylate of the proline moiety of L-captopril forms a hydrogen bond with N346 (ND2−O3, 3.0 Å) and the amide of G325 (N−O2, 2.9 Å). It also makes a strong hydrogen bond with the hydroxyl of Y198 (OH−O3, 2.5 Å), which reaches over from the second subunit of the dimer. The O1 peptide carbonyl oxygen of L-captopril forms a hydrogen bond with a well-ordered water molecule (2.8 Å) that is stabilized by its interaction with R179 (NH2−O, 3.1 Å) and P165 (2.6 Å).

DISCUSSION

EPR spectra of [Co_(*Nm*DapE)] and [Co_(*Hi*DapE)] suggest the first Co(II) ion to bind resides in a distorted tetrahedral coordination geometry at low temperatures, and this assignment is consistent with the crystallographic and MCD data. EPR spectra of [CoCo(*Nm*DapE)] and [CoCo(*Hi*DapE)] suggest a five- or six-coordinate Co(II) ion in the second metal binding site. The EPR data also indicate an antiferromagnetic interaction due to the formation of a spin-coupled species with $|J| > 0.3$ cm^{-1} between the Co(II) ions in [CoCo(*Hi*DapE)] but no interaction was detected in [CoCo(*Nm*DapE)];[24] some 30% of the Co(II) in [CoCo(*Hi*DapE)] is EPR silent. EPR of the L-captopril complexes of both [CoCo(*Nm*DapE)] and [CoCo(*Hi*DapE)] indicated that the hitherto tetrahedral Co(II) ion acquired an additional ligand(s) and modulated the spin coupling in the latter (Figure 2), consistent with the captopril-derived thiolate bridge observed in the crystal structure (Figure 4). For both [CoCo(*Nm*DapE)] and [CoCo(*Hi*DapE)], characteristic MCD bands for high-spin Co(II) in a distorted tetrahedral and distorted octahedral ligand field are observed (Figure 3), consistent with EPR data. An interesting finding is that despite the similarity in the MCD spectra between [CoCo(*Nm*DapE)] and [CoCo(*Hi*DapE)], the spectra obtained for [CoCo(*Nm*DapE)] reveal that both the four- and six-coordinate sites are occupied upon the addition of only 1 equiv of Co(II), suggesting a less than strictly sequential binding model for *Nm*DapE that is not observed for *Hi*DapE. This finding is consistent with EPR data as well as the X-ray crystal structure of [Zn_(*Nm*DapE)].

Correlation of the ZFS observed by MCD with coordination number was used as a coordination number indicator (termed the CN/ZFS correlation). In the CN/ZFS correlation, four-coordinate Co(II) exhibits ZFS < 13 cm^{-1}, also observed directly here by EPR; five-coordinate between 20 and 50 cm^{-1}; and six-coordinate above 50 cm^{-1}.[48] The ZFS parameters determined from fits of VTVH data for [CoCo*Nm*DapE] and [CoCo*Hi*DapE] are consistent with four-coordinate and six-coordinate Co(II) centers in the active site. On the basis of previously published magnetic properties of several μ-aqua μ-hydroxo dicobalt(II) model complexes, weak to moderately strong antiferromagnetic coupling would be expected from a single oxygen atom bridge.[49,50] Fitting of the VTVH data from [CoCo*Nm*DapE] and [CoCo*Hi*DapE] strongly suggests that the bridging oxygen atom, in the resting enzyme, is due to μ-aqua as opposed to μ-hydroxo moieties. MCD data of the L-captopril complexes are consistent with the thiol of L-captopril bridging the two active site Co(II) ions, producing an antiferromagnetically coupled dicobalt(II) center with an $S = 0$ ground state. The overall changes strongly suggest that L-captopril displaces the bridging water molecule and binds to both metal ions through a monatomic bridge whose ligand-field strength is less than that of water. These findings are consistent with EPR data for [CoCo*Hi*DapE] bound by L-captopril. Taken together, the optical, magneto-optical, and EPR results are in strong agreement and indicate that L-captopril interacts directly with both metal ions.

Additional structural information was obtained from X-ray crystallography, including the finding that no active site ligands are displaced upon L-captopril binding except for replacement of the water molecule that bridges the two Zn(II) ions in the wild-type enzyme by the L-captopril-derived thiolate sulfur atom. The remainder of the molecular structure of DapE is barely perturbed, but some significant hydrogen bonds to L-captopril that likely identify residues important for substrate and inhibitor recognition and/or binding are formed. The binding of L-captopril to the dinuclear active site of [ZnZn-(*Nm*DapE)] provides the first structural data for an inhibited form of any DapE enzyme, providing a model for inhibitor design as well as enzyme−substrate interactions.

Inspection of the X-ray crystal structures of [Zn_(*Nm*DapE)] and [ZnZn(*Nm*DapE)], combined with surface analysis, reveals a deep groove that extends along the borders of the catalytic and dimerization domains and houses the active site. This well-defined and negatively charged cavity is shaped from the top by strand β17 and α10 and in the middle by the loop connecting these two elements (residues 321−328). The bottom of the cavity is formed by a loop (residues 132−142) connecting β-strands β6 and α5 and a loop (residues 341−355) connecting β18 and β19. Because the substrate has a linear shape, we predict that it binds in an extended conformation, lining up along the groove with the peptide bond positioned right over the active site metals. DapE enzymes have strict specificity for the L,L-isoform of SDAP.[24] This specificity is built into the active site that includes both the dinuclear metal cluster and adjacent amino acid residues that form a substrate binding cavity groove. Several studies indicate that substrate binding pockets play an important role in substrate recognition and binding for metallohydrolases.[51−53] Insight into the role of this cavity comes from the structure of the [ZnZn(*Nm*DapE)]-L-captopril complex as several interactions between the inhibitor and residues within this cavity are formed. The L-captopril peptide bond forms a hydrogen bond with a well-ordered water molecule, which is stabilized by R179 and P165. In addition, the carboxyl terminus of the dipeptide is held in position by ionic interactions between N346 and G325.

DOI: 10.1021/acs.biochem.5b00475
Biochemistry 2015, 54, 4834−4844

Interestingly, the carboxyl group also forms a hydrogen bond with the hydroxyl moiety of Y198, which resides on the other subunit of the dimer. This interaction is of great interest, because it is the first evidence of a residue from the second subunit interacting with an inhibitor bound to the first subunit. These data suggest a heretofore unknown function for dimer formation of DapE enzymes. Specifically, this indicates that the dimerization domain not only is crucial for dimer formation but also could play an important role in substrate recognition and binding. This is consistent with the findings that dimerization domain deletion mutants of *Hi*DapE are inactive, highlighting the importance of DapE dimer formation.[16]

In summary, a major limitation in developing a previously undescribed class of antimicrobials that target DapE enzymes has been the lack of knowledge about binding of the inhibitor to the DapE active site, including potential residues involved in substrate recognition and binding. We have spectroscopically and crystallographically characterized the binding of the competitive inhibitor L-captopril to DapE. The thiol moiety of L-captopril coordinates to both active site metal ions in a μ-thiolate fashion. No other inhibitor-centered ligands interact with the active site metal ions. Analysis of the first X-ray crystal structure of a DapE enzyme bound to an exogenous ligand, the [ZnZn(*Nm*DapE)]−L-captopril complex, allowed for identification of several important active site pocket residues. These include R179, P165, and N346 that form hydrogen bonds to the functional groups of L-captopril. Remarkably, Y198 from one subunit was discovered to be involved in hydrogen bond formation with the L-captopril bound to the active site of the opposite subunit. This unforeseen hydrogen bonding interaction may be critical for catalysis and may also prove to be crucial in the development of novel medicinal chemistry leads. Because L-captopril is an angiotensin-converting enzyme (ACE) inhibitor and a moderately strong inhibitor of DapE enzymes, understanding the electronic and structural properties of binding of L-captopril to the active site of DapE provides a foundation for the design of new, more potent DapE inhibitors.

■ ASSOCIATED CONTENT

Supporting Information

MCD spectra of *Nm*DapE (Figure SI-1) and *Hi*DapE (Figure SI-2), magnetization plots of the VTVH MCD data (Figures SI-3−SI-12), the structure of $[Co_2(\mu\text{-}OH)(\mu\text{-}1,3\text{-}CF_3COO)_2(Me_3TACN)_2]^+$ and the associated MCD spectrum (Figure SI-13), and the structure of CoF and CoH and the associated MCD spectra (Figure SI-14). The Supporting Information is available free of charge on the ACS Publications website at DOI: 10.1021/acs.biochem.5b00475.

■ AUTHOR INFORMATION

Corresponding Authors

*Department of Chemistry, Marquette University, 535 N. 14th St., Milwaukee, WI 53201-1881. E-mail: richard.holz@marquette.edu. Phone: (414) 288-7230. Fax: (414) 288-7066.

*Center for Structural Genomics of Infectious Diseases, Computation Institute, University of Chicago, 5735 S. Ellis Ave., Chicago, IL 60637. E-mail: andrzejj@anl.gov. Phone: (630) 252-3926. Fax: (630) 252-6991.

Funding

This research has been funded in part by National Institutes of Health Grants R15 AI085559-01A1 (R.C.H.) and GM094585 (A.J.), Contract HHSN272201200026C (A.J.), and Grant P41 EB001980 (B.B.), the U.S. Department of Energy, Office of Biological and Environmental Research, under Contract DE-AC02-06CH11357, National Science Foundation (J.A.L., D.L.S., and W.S.-L.) Grants CHE-0848433, CHE-1303852, and CHE-0820965 (MCD instrument), and the Arnold and Mabel Beckman Foundation (D.L.S.).

Notes

The authors declare no competing financial interest.

■ ACKNOWLEDGMENTS

Results mentioned in this report are derived from work performed at Argonne National Laboratory, Structural Biology Center at the Advanced Photon Source, and at the National Biomedical EPR Center at the Medical College of Wisconsin (MCW). Argonne is operated by University of Chicago Argonne, LLC, for the U.S. Department of Energy, Office of Biological and Environmental Research, under Contract DE-AC02-06CH11357. The MCW EPR Center is funded by National Institutes of Health Grant P41 EB001980 to James S. Hyde.

■ ABBREVIATIONS

L,L-SDAP, *N*-succinyl-L,L-diaminopimelic acid; DapE, *dapE*-encoded *N*-succinyl-L,L-diaminopimelic acid desuccinylase; *m*DAP, *meso*-diaminopimelic acid; Hepes, 4-(2-hydroxyethyl)-1-piperazineethanesulfonic acid; PCR, polymerase chain reaction; IPTG, isopropyl β-D-1-thiogalactopyranoside; NTA, nitrilotriacetic acid; IMAC, immobilized metal affinity chromatography; SDS−PAGE, sodium dodecyl sulfate−polyacrylamide gel electrophoresis; SSM, secondary structure matching algorithm; rmsd, root-mean-square deviation; MCD, magnetic circular dichroism; VTVH, variable-temperature variable-field; EPR, electron paramagnetic resonance; EXAFS, extended X-ray absorption fine structure.

■ REFERENCES

(1) Levy, S. B. (1998) The Challenge of Antibiotic Resistance. *Sci. Am. 278*, 46−53.

(2) Nemecek, S. (1997) Beating Bacteria. New ways to Fend off Antibiotic-Resistant Pathogens. *Sci. Am. 276*, 38−39.

(3) Rice, L. B. (2008) Federal Funding for the Study of Antimicrobial Resistance in Nosocomial Pathogens: No ESKAPE. *J. Infect. Dis. 197*, 1079−1081.

(4) Supuran, C. T., Scozzafava, A., and Clare, B. W. (2002) Bacterial Protease Inhibitors. *Med. Res. Rev. 22*, 329−372.

(5) Scapin, G., and Blanchard, J. S. (1998) Enzymology of Bacterial Lysine Biosyntesis. *Adv. Enzymol. 72*, 279−324.

(6) Coates, A. R. M., and Hu, Y. (2007) Novel approaches to developing new antibiotics for bacterial infections. *Br. J. Pharmacol. 152*, 1147−1154.

(7) Goldman, M. (2011) Reflections on the Innovative Medicines Initiative. *Nat. Rev. Drug Discovery 10*, 321−322.

(8) Born, T. L., Zheng, R., and Blanchard, J. S. (1998) Hydrolysis of *N*-succinyl-L,-L-Diaminopimelic Acid by the *Haemophilus influenzae dapE*-Encoded Desuccinylase: Metal Activation, Solvent Isotope Effects, and Kinetic Mechanism. *Biochemistry 37*, 10478−10487.

(9) Howe, R. A., Bowker, K. E., Walsh, T. R., Feest, T. G., and MacGowan, A. P. (1998) Vancomycin-resistant *Staphylococcus aureus*. *Lancet 351*, 602.

(10) Pavelka, M. S., Jr., and Jacobs, W. R., Jr. (1996) Biosynthesis of Diaminopimelate, the Precursor of Lysine and a Component of Peptidoglycan, is an Essential Function of *Mycobacterium smegmatis*. *J. Bacteriol. 178*, 6496−6507.

(11) Rowsell, S., Pauptit, R. A., Tucker, A. D., Melton, R. G., Blow, D. M., and Brick, P. (1997) Crystal Structure of Carboxypeptidase G2, a

DOI: 10.1021/acs.biochem.5b00475
Biochemistry 2015, 54, 4834−4844

Bacterial Enzyme with Applications in Cancer Therapy. *Structure 5*, 337−347.
(12) Desmarais, W., Bienvenue, D. L., Bzymek, K. P., Petsko, G. A., Ringe, D., and Holz, R. C. (2006) The High-Resolution Structures of the Neutral and the Low pH Crystals of the Aminopeptidase from *Aeromonas proteolytica*. *JBIC, J. Biol. Inorg. Chem. 11*, 398−408.
(13) Gillner, D. M., Bienvenue, D. L., Nocek, B. P., Joachimiak, A., Zachary, V., Bennett, B., and Holz, R. C. (2009) The *dapE*-Encoded *N*-Succinyl-L,L-Diaminopimelic Acid Desuccinylase from *Haemophilus influenzae* Contains two Active Site Histidine Residues. *JBIC, J. Biol. Inorg. Chem. 14*, 1−10.
(14) Gillner, D., Armoush, N., Holz, R. C., and Becker, D. P. (2009) Inhibitors of bacterial N-succinyl-l,l-diaminopimelic acid desuccinylase (DapE) and demonstration of in vitro antimicrobial activity. *Bioorg. Med. Chem. Lett. 19*, 6350−6352.
(15) Gillner, D., Becker, D., and Holz, R. (2013) Lysine biosynthesis in bacteria: a metallodesuccinylase as a potential antimicrobial target. *JBIC, J. Biol. Inorg. Chem. 18*, 155−163.
(16) Nocek, B. P., Gillner, D. M., Fan, Y., Holz, R. C., and Joachimiak, A. (2010) Structural Basis for Catalysis by the Mono- and Dimetalated Forms of the *dapE*-Encoded *N*-succinyl-L,L-Diaminopimelic Acid Desuccinylase. *J. Mol. Biol. 397*, 617−626.
(17) Karita, M., Etterbeek, M. L., Forsyth, M. H., Tummuru, M. R., and Blaser, M. J. (1997) Characterization of *Helicobacter pylori* DapE and Construction of a Conditionally Lethal DapE Mutant. *Infect. Immun. 65*, 4158−4164.
(18) Jacobsen, F. E., Lewis, J. A., and Cohen, S. M. (2007) The Design of Inhibitors for Medically Relevant Metalloproteins. *ChemMedChem 2*, 152−171.
(19) Cosper, N. J., Bienvenue, D. L., Shokes, J. E., Gilner, D. M., Tsukamoto, T., Scott, R., and Holz, R. C. (2003) The dapE-Encoded *N*-succinyl-L,L-Diaminopimelic Acid Desuccinylase from H*aemophilus influenzae* is a Dinuclear Metallohydrolase. *J. Am. Chem. Soc. 125*, 14654−14655.
(20) Lin, Y., Myhrman, R., Schrag, M. L., and Gelb, M. H. (1988) Bacterial *N*-succinyl-L-Diaminopimelic Acid Desuccinylase. Purification, Partial Characterization, and Substrate Specificity. *J. Biol. Chem. 263*, 1622−1627.
(21) Nocek, B., Starus, A., Makowska-Grzyska, M., Gutierrez, B., Sanchez, S., Jedrzejczak, R., Mack, J. C., Olsen, K. W., Joachimiak, A., and Holz, R. C. (2014) The Dimerization Domain in DapE Enzymes Is required for Catalysis. *PLoS One 9*, e93593.
(22) Aslanidis, C., and de Jong, P. J. (1990) Ligation-independent cloning of PCR products (LIC-PCR). *Nucleic Acids Res. 18*, 6069−6074.
(23) Kim, Y., Babnigg, G., Jedrzejczak, R., Eschenfeldt, W. H., Li, H., Maltseva, N., Hatzos-Skintges, C., Gu, M., Makowska-Grzyska, M., Wu, R., An, H., Chhor, G., and Joachimiak, A. (2011) High-throughput protein purification and quality assessment for crystallization. *Methods 55*, 12−28.
(24) Bienvenue, D. L., Gilner, D. M., Davis, R. S., Bennett, B., and Holz, R. C. (2003) Substrate Specificity, Metal Binding Properties, and Spectroscopic Characterization of the *dapE*-Encoded-*N*-succinyl-L,L-Diaminopimelic Acid Desuccinylase from *Haemophilus influenzae*. *Biochemistry 42*, 10756−10763.
(25) Bergmann, M., and Stein, W. H. (1939) Naphthalene-β-sulfonic acid as a reagent for amino acids. *J. Biol. Chem. 129*, 609−618.
(26) D'souza, V. M., and Holz, R. C. (1999) The Methionyl Aminopeptidase from *Escherichia coli* is an Iron(II) Containing Enzyme. *Biochemistry 38*, 11079−11085.
(27) Riley, M. J. (2008) *VTVH 2.1.1 Program for the Simulation and Fitting Variable Temperature−Variable Field MCD Spectra*, The University of Queensland, Brisbane, Australia.
(28) Ely, F., Hadler, K., Mitić, N., Gahan, L., Ollis, D., Plugis, N., Russo, M., Larrabee, J., and Schenk, G. (2011) Electronic and geometric structures of the organophosphate-degrading enzyme from Agrobacterium radiobacter (OpdA). *JBIC, J. Biol. Inorg. Chem. 16*, 777−787.
(29) Paulat, F. L. N., and Lehnert, N. (2008) Detailed Assignment of the Magnetic Circular Dichroism and UVvis Spectra of Five-Coordinate High-Spin Ferric [Fe(TPP)(Cl)]. *Inorg. Chem. 47*, 4963−4976.
(30) Nocek, B., Mulligan, R., Bargassa, M., Collart, F., and Joachimiak, A. (2008) Crystal structure of aminopeptidase N from human pathogen Neisseria meningitides. *Proteins: Struct., Funct., Genet. 70*, 273−279.
(31) Rosenbaum, G., Alkire, R. W., Evans, G., Rotella, F. J., Lazarski, K., Zhang, R.-G., Ginell, S. L., Duke, N., Naday, I., Lazarz, J., Molitsky, M. J., Keefe, L., Gonczy, J., Rock, L., Sanishvili, R., Walsh, M. A., Westbrook, E., and Joachimiak, A. (2006) The Structural Biology Center 19ID undulator beamline: facility specifications and protein crystallographic results. *J. Synchrotron Radiat. 13*, 30−45.
(32) Minor, W., Cymborowski, M., Otwinowski, Z., and Chruszcz, M. (2006) HKL-3000: the integration of data reduction and structure solution - from diffraction images to an initial model in minutes. *Acta Crystallogr., Sect. D: Biol. Crystallogr. 62*, 859−866.
(33) Emsley, P. C. K. (2004) Coot: model-building tools for molecular graphics. *Acta Crystallogr., Sect. D: Biol. Crystallogr. 60*, 2126−2132.
(34) Murshudov, G. N., Vagin, A. A., and Dodson, E. J. (1997) Refinement of Macromolecular Structures by the Maximum-Likelihood Method. *Acta Crystallogr., Sect. D: Biol. Crystallogr. 53*, 240−255.
(35) Adams, P. D., Afonine, P. V., Bunkóczi, G., Chen, V. B., Davis, I. W., Echols, N., Headd, J. J., Hung, L.-W., Kapral, G. J., Grosse-Kunstleve, R. W., McCoy, A. J., Moriarty, N. W., Oeffner, R., Read, R. J., Richardson, D. C., Richardson, J. S., Terwilliger, T. C., and Zwart, P. H. (2010) PHENIX: a comprehensive Python-based system for macromolecular structure solution. *Acta Crystallogr., Sect. D: Biol. Crystallogr. 66*, 213−221.
(36) Laskowski, R. A., MacArthur, M. W., Moss, D. S., and Thornton, J. M. (1993) PROCHECK: a program to check the stereochemical quality of protein structures. *J. Appl. Crystallogr. 26*, 283−291.
(37) Davis, I. W., Leaver-fay, A., Chen, V. B., Block, J. N., Kapral, G. J., Wang, X., Murray, L. W., Arendall, W. B., Snoeyink, J., Richardson, J. S., and Richardson, D. C. (2007) MolProbity: all-atom contacts and structure validation for proteins and nucleic acids. *Nucleic Acids Res. 35*, W375−W383.
(38) Eufri, D. S. A., and Sironi, A. (1989) Smile - Shaded Molecular imaging on low-cost equipment. *J. Mol. Graphics 7*, 184.
(39) Bennett, B. (2010) EPR of Cobalt-Substituted Zinc Enzymes. In Metals in Biology: Applications of High Resolution EPR to Metalloenzymes. In *Biological Magnetic Resonance, Metals in Biology* (Hanson, G., and Berliner, L., Eds.) pp 345−370, Springer, New York.
(40) Larrabee, J. A., Schenk, G., Mitic, N., and Riley, M. J. (2015) Use of magnetic circular dichroism to study dinuclear metallohydrolases and the corresponding biomimetics. *Eur. Biophys. J.*, DOI: 10.1007/s00249-015-1053-6.
(41) Kaden, T. A., Holmquist, B., and Vallee, B. L. (1974) Magnetic circular dichroism of cobalt(II) complexes. *Inorg. Chem. 13*, 2585−2590.
(42) Larrabee, J. A., Alessi, C. M., Asiedu, E. T., Cook, J. O., Hoerning, K. R., Klingler, L. J., Okin, G. S., Santee, S. G., and Volkert, T. L. (1997) Magnetic circular dichroism spectroscopy as a probe of geometric and electronic structure of cobalt(II)-substituted proteins: Ground-state zero-field splitting as a coordination number indicator. *J. Am. Chem. Soc. 119*, 4182−4196.
(43) Harding, M. J., and Briat, B. (1973) The electronic absorption and magnetic circular dichroism spectra of cobalt (II) bromate hexahydrate. *Mol. Phys. 25*, 745−776.
(44) Daumann, L. J., Comba, P., Larrabee, J. A., Schenk, G., Stranger, R., Cavigliasso, G., and Gahan, L. R. (2013) Synthesis, Magnetic Properties, and Phosphoesterase Activity of Dinuclear Cobalt(II) Complexes. *Inorg. Chem. 52*, 2029−2043.
(45) Larrabee, J. A., Chyun, S.-A., and Volwiler, A. S. (2008) Magnetic Circular Dichroism Study of a Dicobalt(II) Methionine

DOI: 10.1021/acs.biochem.5b00475
Biochemistry 2015, 54, 4834−4844

Aminopeptidase/Fumagillin Complex and Dicobalt II−II and II−III Model Complexes†. *Inorg. Chem. 47*, 10499−10508.
(46) Larrabee, J. A., Johnson, W. R., and Volwiler, A. S. (2009) Magnetic Circular Dichroism Study of a Dicobalt(II) Complex with Mixed 5- and 6-Coordination: A Spectroscopic Model for Dicobalt(II) Hydrolases. *Inorg. Chem. 48*, 8822−8829.
(47) Badger, J., Sauder, J. M., Adams, J. M., Antonysamy, S., Bain, K., Bergseid, M. G., Buchanan, S. G., Buchanan, M. D., Batiyenko, Y., Christopher, J. A., Emtage, S., Eroshkina, A., Feil, I., Furlong, E. B., Gajiwala, K. S., Gao, X., He, D., Hendle, J., Huber, A., Hoda, K., Kearins, P., Kissinger, C., Laubert, B., Lewis, H. A., Lin, J., Loomis, K., Lorimer, D., Louie, G., Maletic, M., Marsh, C. D., Miller, I., Molinari, J., Muller-Dieckmann, H. J., Newman, J. M., Noland, B. W., Pagarigan, B., Park, F., Peat, T. S., Post, K. W., Radojicic, S., Ramos, A., Romero, R., Rutter, M. E., Sanderson, W. E., Schwinn, K. D., Tresser, J., Winhoven, J., Wright, T. A., Wu, L., Xu, J., and Harris, T. J. R. (2005) Structural analysis of a set of proteins resulting from a bacterial genomics project. *Proteins: Struct., Funct., Genet. 60*, 787−796.
(48) Makinen, M. W., and Yim, M. B. (1981) Coordination environment of the active-site metal ion of liver alcohol dehydrogenase. *Proc. Natl. Acad. Sci. U. S. A. 78*, 6221−6225.
(49) Turpeinen, U., Ahlgren, M., and Hämäläinen, R. (1982) Structures of di-μ-acetato-(O,O′)-μ-aqua-bis[acetato(N,N,N′,N′-tetramethylethylenediamine)cobalt(II) and μ-aqua-di-μ-chloroacetato-(O,O′)-bis[chloroacetato(N,N,N′,N′-tetramethylethylenediamine)-cobalt(II). *Acta Crystallogr., Sect. B: Struct. Crystallogr. Cryst. Chem. 38*, 1580−1583.
(50) Chaudhuri, P., Ouerbach, J., Wieghardt, K., Nuber, B., and Weiss, J. (1990) Synthesis, electrochemistry, and magnetic properties of binuclear cobalt complexes containing the $Co_2(\mu\text{-}X)(\mu\text{-carboxylato})_2^{+n}$ core (X=OH, Cl, or Br; n=1−3). *J. Chem. Soc., Dalton Trans.*, 271−278.
(51) Ustynyuk, L., Bennett, B., Edwards, T., and Holz, R. C. (1999) Inhibition of the Aminopeptidase from *Aeromonas proteolytica* by Aliphatic Alcohols. Characterization of the Hydrophobic Substrate Recognition Site. *Biochemistry 38*, 11433−11439.
(52) Chen, G., Edwards, T., D'souza, V. M., and Holz, R. C. (1997) Mechanistic studies on the aminopeptidase from *Aeromonas proteolytica*: A two-metal ion mechanism for peptide hydrolysis. *Biochemistry 36*, 4278−4286.
(53) Lowther, W. T., and Matthews, B. W. (2002) Metalloaminopeptidases: Common Functional Themes in Disparate Structural Suroundings. *Chem. Rev. 102*, 4581−4607.

DOI: 10.1021/acs.biochem.5b00475
Biochemistry 2015, 54, 4834−4844